Journal of Ceramic Processing Research. Vol. 23, No. 2, pp. 199~207 (2022)
(Received 28 October 2021, Received in revised form 30 December 2021, Accepted 10 January 2022)
https://doi.org/10.36410/jcpr.2022.23.2.199

J O U R N A L O F
Ceramic Processing Research

Quenching process effects on the performance of a TiO_2 photoelectrode for dye-sensitized solar cells

Woon-Yong Park[a] and Ki-Tae Lee[a,b,c,*]
[a]*Division of Advanced Materials Engineering, Jeonbuk National University, Jeonbuk 54896, Republic of Korea*
[b]*Department of Energy Storage/Conversion Engineering of Graduate School (BK21 FOUR), Jeonbuk National University, Jeonbuk 54896, Republic of Korea*
[c]*Hydrogen and Fuel Cell Research Center, Jeonbuk National University, Jeonbuk 54896, Republic of Korea*

A rapid cooling (quenching) step has been introduced in fabrication of TiO_2 photoelectrodes for dye-sensitized solar cells (DSSCs). The quenching process, studied at a fixed sintering temperature, decreased particle size but increased surface roughness without any substantial change in the crystal structure or oxidation state of TiO_2 films. Therefore, the change in the DSSC performance induced by the quenching was related closely to the microstructural and morphological changes in the TiO_2 films. Smaller particle size and the rough surface of TiO_2 films facilitated dye adsorption and increased the number of active reaction sites. In particular, the enlarged number of active reaction sites produced by the quenching process promoted the charge transfer reaction at the TiO_2-dye-electrolyte interface, resulting in overall performance improvement of DSSCs. The conversion efficiency of the furnace cooled- and quenched-TiO_2 films at 500 °C were 4.588% and 5.797%, respectively.

Keywords: Dye-sensitized solar cells, Photoelectrode, TiO_2, Sintering process, Quenching method.

Introduction

Dye-sensitized solar cells (DSSCs) are a promising technological advancement due to their conversion efficiency, low-cost fabrication process, and diverse applicability compared to conventional silicon-based solar cells [1-3]. The structure of a DSSC is composed of photoelectrode, dye sensitizer, electrolyte, counter electrode, and transparent conducting substrate. Electrons are generated by excited-dye molecules adsorbed on the surface of the photoelectrode with incident light and move toward the photoelectrode or electrolyte [4-7]. Various efforts such as electrode surface morphology control [8-12], dopants in the electrode [13-15], development of advanced dyes [16-18], and electrolytes [19, 20] have aimed to improve the performance of DSSCs.

The photoelectrode in a DSSC plays a key role in enhancing the diffusion of electrons and adsorbing a large number of dye molecules at the electrode surfaces [21-23]. Therefore, the photoelectrode layer usually is fabricated in the form of a mesoporous film with a large surface area to promote efficient light harvesting and a large amount of photo-generation [24]. Meanwhile, TiO_2 is one of the most suitable materials to satisfy photoelectrode conditions in DSSCs because of its large band gap (anatase: 3.2 eV, rutile: 3.0 eV), suitable band edge levels for charge injection/extraction, non-toxicity, and low cost [25-28].

Generally, it is advantageous to reduce the particle size of TiO_2 in the photoelectrode because more dye molecules can be adsorbed at the extended surface area [7]. However, the reduction of particle size leads to an increase in defects at the boundary [29, 30]. Cao et al. reported that particle size and surface area in the mesoporous films strongly affect electron-hole generation and charge transport from dye to TiO_2 particles in the photoelectrode [31, 32]. Yanagida et al. reported that particle size and surface area of TiO_2 are major factors that affect the electron diffusion coefficient and recombination lifetime [33, 34]. Yang et al. reported that particles with a hollow hemisphere structure can increase the amount of dye adsorption and electron collection efficiency by inducing the light scattering [35]. Meanwhile, the dispersed micro/nano-sized noble metal particles (Au, Ag etc.) in metal oxide nanoparticles can improve the performance of DSSCs by plasmonic resonance effect of electrons on the material surface with respect to incident light [36-38]. In this regard, it is important to control the microstructure, such as particle size and surface morphology, of TiO_2 photoelectrode to improve the performance of DSSCs. The microstructure can be controlled by manufacture process such as deposition methods for the fabrication of mesoporous films (doctor blading, screen printing, spin coating, etc.), sintering process (temperature, holding time, heating/cooling rate). It is known that the

*Corresponding author:
Tel : +82-63-270-2290
Fax: +82-63-270-2386
E-mail: ktlee71@jbnu.ac.kr

rapid cooling (quenching) process can maintain high temperature phase even at room temperature and suppress the grain growth [39-41]. Especially, it has been reported that TiO_2 photoelectrode with small grain size showed much better DSSC performance than that with large grain size [42-45].

In this work, we introduced a rapid cooling (quenching) step into the conventional sintering process to modify the microstructure and surface morphology of the TiO_2 photoelectrode. The quenching process at various temperatures was conducted to investigate the changes in microstructure and surface morphology. The correlation between performance and change in the microstructure driven by the quenching process was investigated. Unlike the conventional sintering process, the quenching treatment in the sintering process increased the surface area of TiO_2 and yielded a larger number of adsorption sites during dye infiltration, resulting in performance improvement of the DSSCs.

Experimental Procedure

Preparation of TiO_2 photoelectrode

Fluorine-doped tin oxide (FTO)-coated glass (TEC 8, Pilkington, UK) with a sheet resistance of 6-9 Ω/□ was cleaned using acetone (99.5%, Daejung Chemicals and Metals Co., Korea), 2-propanol (99+%, Alfa Aesar, USA), and DI-water for an interval of 10 min per solvent and then dried using an air gun. A screen printing method was used with TiO_2 paste (Ti-Nanoixde T/SP, Solaronix, Switzerland) for deposition of mesoporous TiO_2 films. The screen-printed samples were sintered at 500 °C for 30 min in a tube furnace in an ambient atmosphere as shown in Fig. 1. The heating rate was adjusted by 10 °C/min. In conventional cooled (named to "furnace cooled"), The furnace was set to drop from 500 °C to room temperature in 3 hours. Unlike the conventional furnace cooling step, in the quenching step, the sliding furnace was pushed to expose to room temperature atmosphere after finishing the sintering step. The final thickness of TiO_2 films was approximately 9 μm. Meanwhile, the sintering temperature was varied at 400, 450, and 500 °C to investigate the sintering temperature effect.

Fabrication of DSSCs

The prepared mesoporous TiO_2 films were immersed in a prepared 0.3 mM (bis(tetrabutylammonium)-cis-di(thiocyanato)-N,N'–bis(4-carboxylato-4'-carboxylic acid-2,2-bipyridine) ruthenium (II) (N719, Solaronix, Switzerland) ethanol-based solution in a dark field at room temperature for 24 h. For the counter electrode, Pt was deposited on indium-doped tin oxide (ITO)-coated glass (STN 10, UID, Korea) with a sheet resistance of 6-9 Ω/□ using DC sputtering equipment (E-1030, Hitachi, Japan) at 25 mA for 30 s. The thickness of the deposited Pt was approximately 5 nm.

The DSSC cells were assembled by attaching the

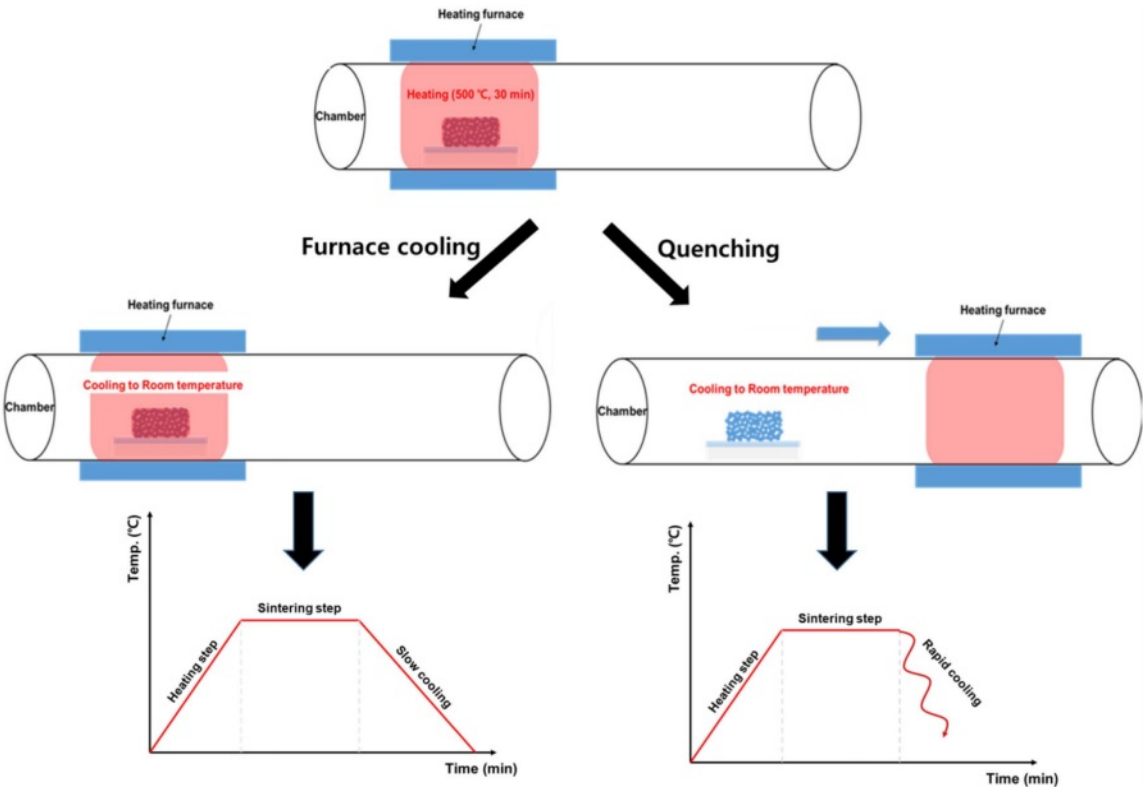

Fig. 1. (a) Schematic diagram of the air quenching process compared to the conventional furnace-cooling process.

photoelectrode and the counter electrode such that they faced one another. A 60-μm-thick Surlyn film (Solaronix, Switzerland) was used as a sealant. An electrolyte with an iodide/tri-iodide (I^-/I^{3-}) redox couple in acetonitrile solvent (AN-50, Solaronix, Switzerland) was injected through the holes on the counter electrode. The active area of the TiO_2 photoelectrode and electrolyte was 0.25 cm^2 and 1.2 cm^2, respectively.

Characterization and performance evaluation

X-ray diffraction (XRD) was carried out using an X-ray diffractometer (X'Pert Pro Powder, PANalytical, Netherlands) with Cu Kα radiation to analyze phases and crystal structure. Diffraction patterns were recorded at a scan rate of 4°/min over a 2θ range of 20 to 70°. X-ray photoelectron spectroscopy (XPS) was performed using a surface analysis spectrometer (AXIS Nova, Kratos Analytical Ltd., UK) with a monochromatic Al Kα source to verify the valence state of Ti in the samples. The microstructure and surface morphology of TiO_2 thin films were analyzed by a high resolution-scanning electron microscope (HR-SEM, SU8230, Hitachi, Japan) and an atomic force microscope (AFM, Nanoscope III, Veeco Instrument Inc., USA), respectively. Ultraviolet-visible (UV-Vis) spectroscopy was performed by UV-vis spectrometry (HP 8453, Hewlett Packard, USA) to analyze the dye absorption according to the cooling method change.

Current-voltage (I-V) characteristics of DSSCs were obtained under a standard illumination condition (100 mW/cm^2 AM 1.5G) using a source meter (Keithely 2400, Tekronix Inc., USA) in the range of ±1 V, at a scan step of 0.02 V and delay time of 0.50 s. Electrochemical impedance spectroscopy (EIS) analysis was carried out using a potentiostat (SP150, Biologic SAS, France) with a frequency range of 9 mHz to 100 kHz to confirm the change of the electrochemical component in the DSSCs. The results of the I-V curve and EIS spectra were analyzed with the average values of at least six individual cells.

Results and Discussion

Crystallographic phases of mesoporous TiO_2 films sintered at 500 °C are shown in Fig. 2. The TiO_2 anatase phase (JCPDS 73-1764) and SnO_2 phase (JCPDS 46-1088) were observed in both the furnace-cooled and quenched samples. The SnO_2 phase comes from the FTO substrate. Based on the XRD patterns, no significant change in characteristic diffraction peaks was created due to the rapid cooling, which indicates that the quenching step during the sintering process did not induce any substantial change in the crystal structure of TiO_2.

XPS analysis was performed to confirm the valence states of Ti in the TiO_2 films because dye adsorption can be affected by the electronic structure of the TiO_2 photoelectrode. The Ti2p core-level spectra consisted of stoichiometric doublet peaks from spin-orbit splitting corresponding to $Ti2p_{3/2}$ and $Ti2p_{1/2}$ states at 458.8 and 464.5 eV, respectively, as shown in Fig. 3. Upon fitting

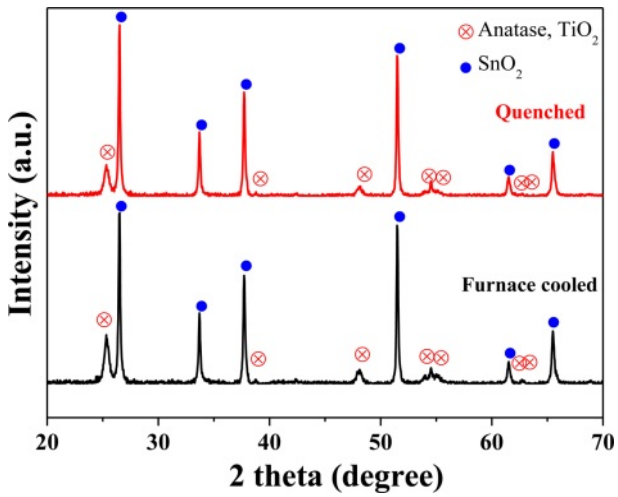

Fig. 2. X-ray diffraction patterns of the furnace-cooled and quenched TiO_2 films at 500 °C.

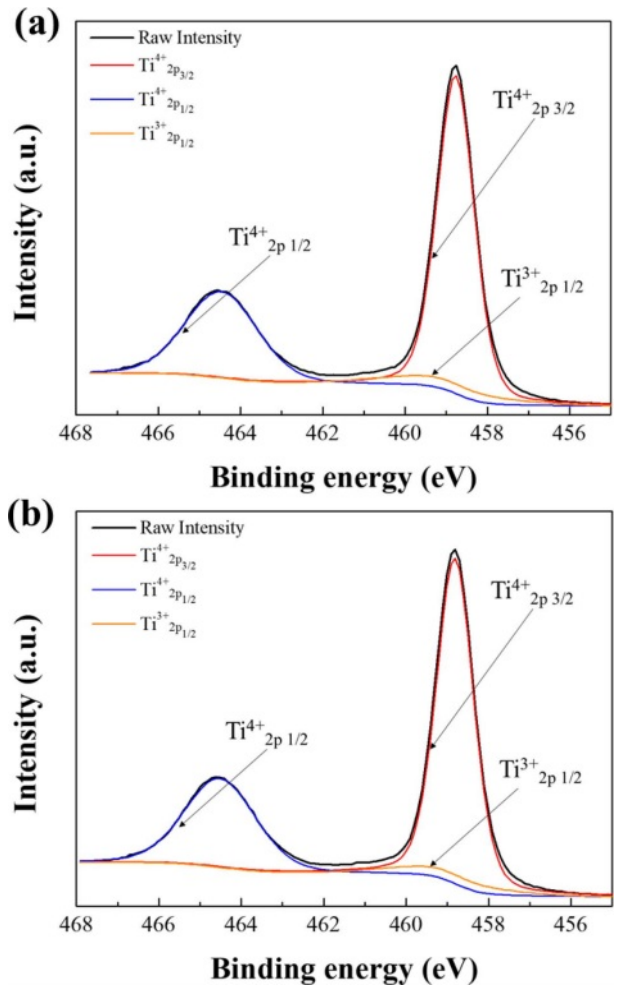

Fig. 3. Ti2p core-level spectra of the (a) furnace-cooled and (b) quenched TiO_2 films at 500 °C.

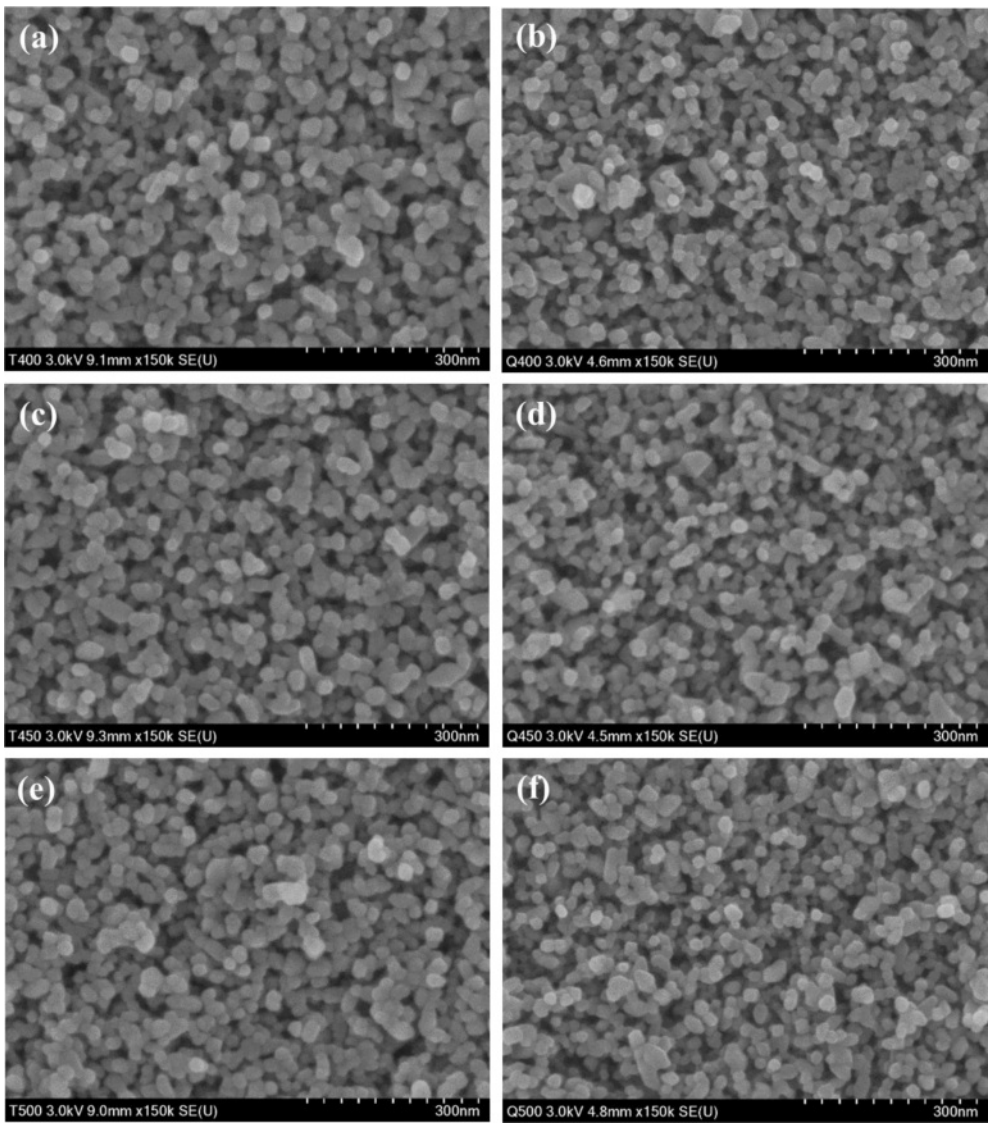

Fig. 4. HR-SEM surface images of (a, c, e) furnace-cooled and (b, d, f) quenched TiO_2 films at various sintering temperatures; (a, b) 400 °C, (c, d) 450 °C, and (e, f) 500 °C.

by a Gaussian method, the shoulder peak of $Ti^{3+}2p1/2$ at 459.1 eV as well as stoichiometric doublet peaks of $Ti^{4+}2p_{3/2}$ and $Ti^{4+}2p_{1/2}$ were observed. This indicates that TiO_2 and Ti_2O_3 coexist in the as-deposited TiO_2 films. Moreover, no peak shift was observed, and the peak areas were similar between the furnace-cooled sample and the quenched sample. Thus, the XPS analysis showed that the surface oxidation state and chemical bonding of TiO_2 films are not affected by a quenching step during the sintering process.

The HR-SEM images of the furnace-cooled and quenched TiO_2 films at various sintering temperatures are shown in Fig. 4. Porous TiO_2 films with nanometer-sized spherical particle necking were formed. Unlike the XRD and XPS data, microstructural changes in the TiO_2 film were observed according to presence of the quenching process. The quenched TiO_2 films had smaller particles compared to the furnace-cooled TiO_2 films.

The ImageJ processing program was used to quantify the distribution of TiO_2 particle size from the HR-SEM images. Fig. 5 shows the particle size distributions of the furnace-cooled and quenched TiO_2 films at various sintering temperatures, and the calculated average particle diameters are listed in Table 1. The average particle size of the samples increased with sintering temperature, as shown in Fig. 5 and Table 1. However, the quenched TiO_2 films had a smaller average particle diameter than did the furnace-cooled TiO_2 films at the same sintering temperature. This indicates that it is possible to induce an increase in the nano-sized void while maintaining the overall photoelectrode structure by introduction of a quenching process. Therefore, decrease in particle size of TiO_2 can lead to an expansion of the adsorption site of the dye molecules and consequently increase the amount of dye loading.

AFM images of the furnace-cooled and quenched

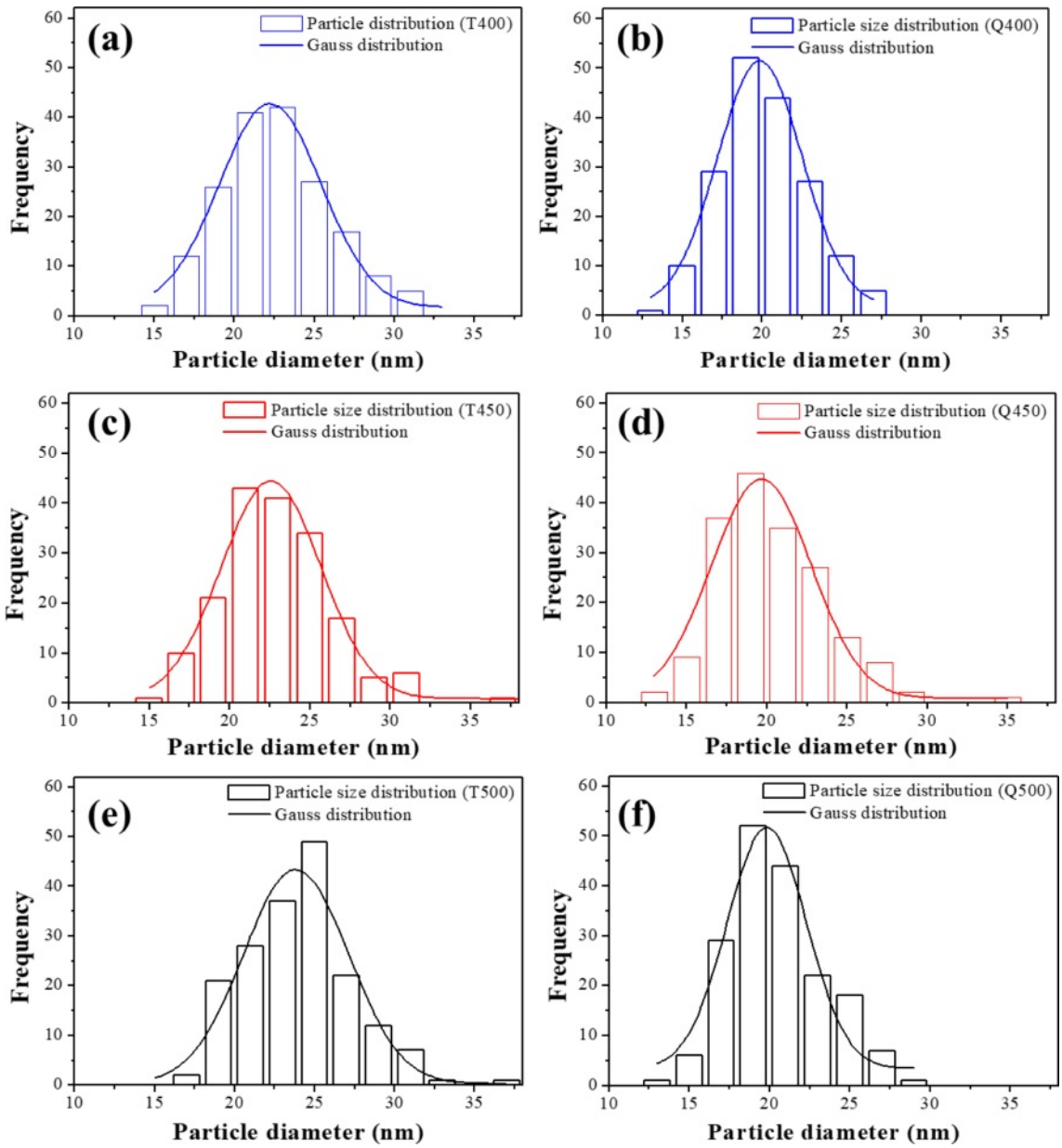

Fig. 5. Particle size distributions of (a, c, e) furnace-cooled and (b, d, f) quenched TiO_2 films at various sintering temperatures; (a, b) 400 °C, (c, d) 450 °C, and (e, f) 500 °C.

Table 1. Calculated average particle diameters of furnace-cooled and quenched TiO_2 films at various sintering temperatures.

Sample	Average particle diameter (nm)		
	400 °C	450 °C	500 °C
Furnace cooled TiO_2	22.59	23.03	23.92
Quenched TiO_2	20.03	20.29	20.48

TiO_2 films at 500 °C are shown in Fig. 6. The quenched TiO_2 film had a relatively rough surface with higher root-mean-square roughness (RMS) values than the furnace-cooled TiO_2 film. The rough surface can enhance the active reaction area by expanding the interface between the electrolyte and the photoelectrode.

I-V characteristic measurement confirmed the performance according to change in the sintering process (Fig. 7), and the parameters are listed in Table 2. All the quenched samples showed better performance than the furnace-cooled samples at the same sintering temperature. The sample quenched at 500 °C exhibited the highest conversion efficiency of 5.797%. This performance is comparable with those of several studies (Table 2) [46-49]. The short-circuit current density (I_{SC}) of the quenched samples increased significantly compared to that of the furnace-cooled samples. Generally, dyes are a key component for improvement of DSSC performance because they generate electrons when sunlight is incident on the device. Therefore, the amount of dye adsorbed on mesoporous TiO_2 films is an impor-

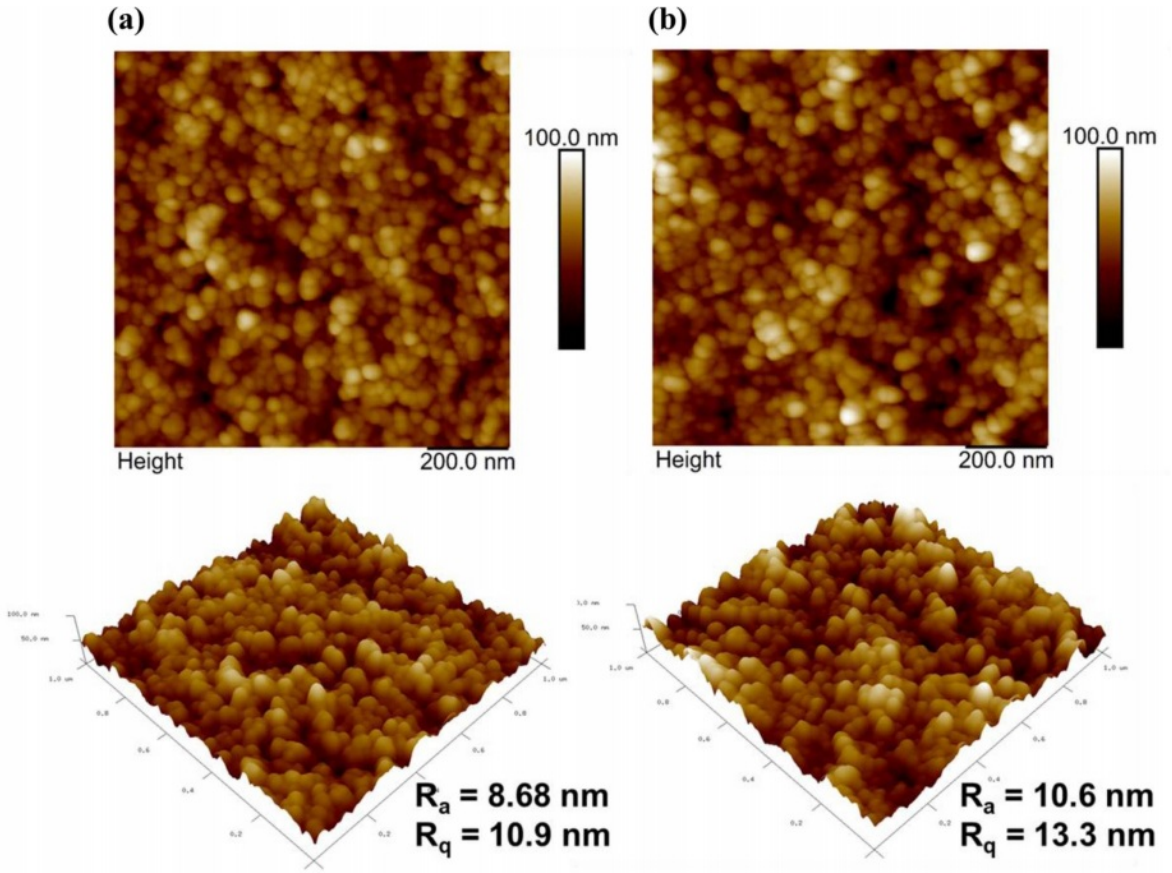

Fig. 6. AFM images of the (a) furnace-cooled and (b) quenched TiO_2 films at 500 ºC.

tant factor in generation and movement of electrons, which directly affects the current density and efficiency. Meanwhile, since the electricity generation mechanism of DSSCs is related closely to the electrochemical reactions, the charge transfer reaction at the TiO_2-dye-electrolyte interface, which is defined as a triple phase boundary, is a critical performance factor. The electrochemical charge transfer reaction strongly depends on the number of active reaction sites. As the number of active reaction sites increases, the charge transfer reaction proceeds more actively. Therefore, the small particle size and rough surface morphology according to introduction of the quenching process, as shown in Table 1 and Fig. 6, can increase the amount of dye loading and promote the charge transfer reaction, thereby improving the performance.

UV-visible spectroscopy analysis was performed to compare the adsorption amount of N719 dye according to sintering process of the TiO_2 photoelectrode (Fig. 8). The quenched TiO_2 film showed higher absorbance in the 525-535 nm wavelength range corresponding to the N719 dye molecule compared with the furnace-cooled TiO_2 film. This indicates that the amount of dye adsorption increased by introduction of the quenching process.

EIS analysis was used to confirm the relationship between performance of the DSSCs and electrochemical

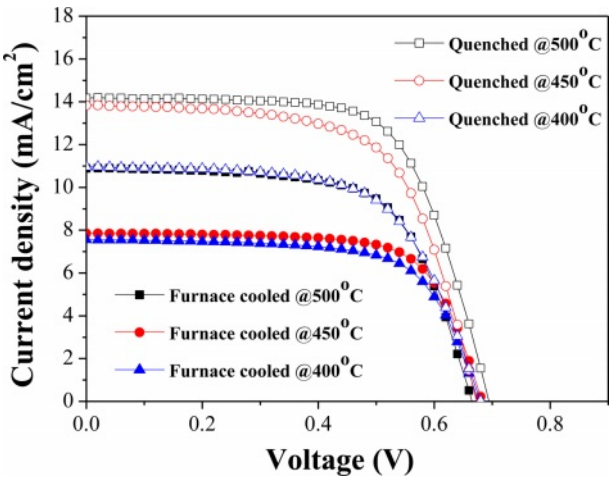

Fig. 7. Photocurrent density-voltage curves of DSSCs with the furnace-cooled- and quenched TiO_2 films at various temperatures.

reaction. AC impedance spectra of DSSCs with the furnace-cooled and quenched TiO_2 films at various temperatures are shown in Fig. 9. In general, there are typically three distinct semicircles on the Nyquist plots of DSSCs. The first semicircle in the high-frequency range, the second semicircle in the middle-frequency range, and the third semicircle in the low-frequency range are designated to redox reaction of $3I^-/I^{3-}$ at the

Table 2. Short-circuit current (I_{SC}), open-circuit voltage (V_{OC}), fill factor (FF), and power-conversion efficiency (η) of the DSSCs according to sintering method.

Sample	V_{OC} (V)	I_{SC} (mA/cm^2)	FF (%)	η (%)
Furnace cooled at 500 °C	0.665±0.004	10.342±0.685	66.84±0.88	4.588±0.232
Quenched at 500 °C	0.676±0.004	12.923±0.630	66.41±0.34	5.797±0.240
Furnace cooled at 450 °C	0.691±0.010	7.362±0.335	71.70±0.68	3.641±0.081
Quenched at 450 °C	0.682±0.007	11.810±0.509	67.91±0.88	5.465±0.113
Furnace cooled at 400 °C	0.679±0.002	7.110±0.283	69.94±1.05	3.374±0.076
Quenched at 400 °C	0.672±0.006	10.066±0.561	64.21±1.20	4.337±0.203
Hydrothemal TiO_2 [31]	0.7111	11.34	66.57	5.7
Flame spray pyrolysis TiO_2 [32]	0.72	5.25	64	2.44
O_2 plasma treatment of TiO_2 [33]	0.80	7.59	66	4.0
Aerosol deposition TiO_2 [34]	0.72	8.08	69.41	4.07

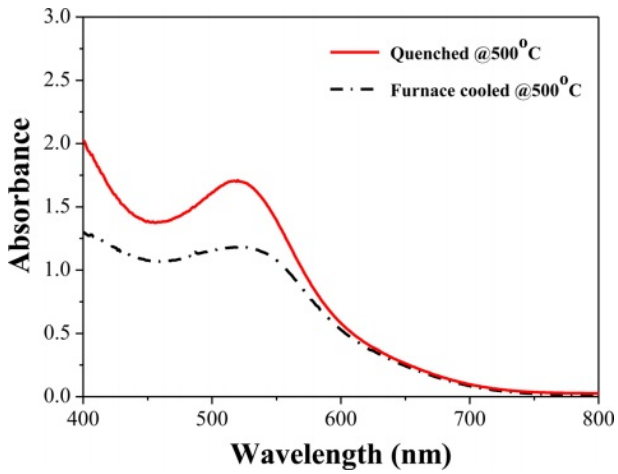

Fig. 8. UV-visible spectroscopy of N719-absorbed TiO_2/FTO/glass samples.

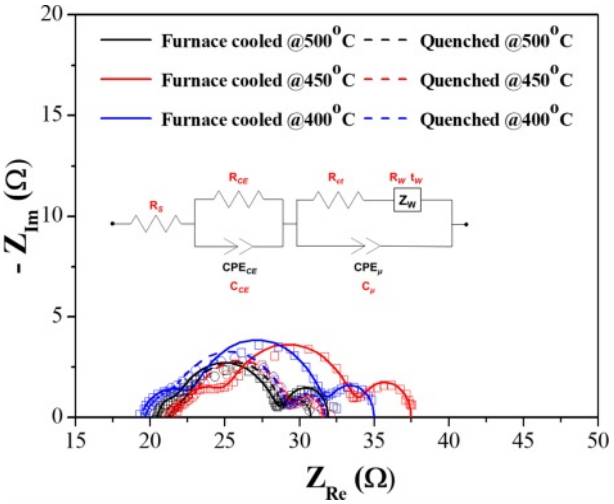

Fig. 9. AC impedance spectra of DSSCs with the furnace-cooled and quenched TiO_2 films at various temperatures (Dot: Raw data, Line: fitting data from an equivalent circuit).

Pt counter electrode (R_{CE}), charge transfer reaction at the interface between TiO_2/N719 and electrolyte (R_{ct}), and Warburg diffusion process of iodide (R_w), respectively [50-52]. The electrochemical parameters obtained by simulation of fitting between equivalent circuit and impedance spectra from Fig. 9 are listed in Table 3. The measured impedance data (blank dots) are well matched with the simulated data (lines) calculated by the equivalent circuit. Therefore, the calculated electrochemical parameters could be meaningful. As shown in Fig. 9, the size of the second semicircle for all the quenched samples decreased significantly compared with the furnace-cooled samples at the same sintering temperature. Similarly, the resistance values of charge transfer (R_{ct}) and diffusion process (R_w) for all the quenched samples decreased compared with those of the furnace-cooled samples (Table 3). This result is consistent with the tendency of I_{SC} and efficiency in I-V characteristics. Namely, introduction of the quenching process might facilitate the charge transfer reaction and diffusion process. It is also reported that the second semicircle decreases when the number of electrons generated increases [52]. As mentioned on the I-V

Table 3. Electrochemical resistance and capacitance values of illuminated DSSCs of the TiO_2 photoelectrode according to sintering method under open circuit conditions. Data were obtained from EIS fits using the equivalent circuits in Fig. 9.

Sample	R_S (Ω)	R_{CE} (Ω)	C_{CE} (mF)	R_{ct} (Ω)	C_μ (mF)	R_W (Ω)	t_W (s)
Furnace cooled at 500 °C	21.305±1.606	2.683±0.740	0.138±0.093	5.204±0.945	0.233±0.114	2.994±0.346	2.321±0.683
Quenched at 500 °C	21.260±0.75	1.167±0.179	0.069±0.015	5.031±0.575	0.387±0.033	1.987±0.202	1.373±0.333
Furnace cooled at 450 °C	21.057±1.752	3.420±0.115	0.006±0.001	8.547±0.101	0.256±0.021	4.023±0.129	1.263±0.189
Quenched at 450 °C	20.197±0.539	2.004±0.312	0.030±0.007	6.731±0.249	0.316±0.016	2.352±0.304	0.970±0.072
Furnace cooled at 400 °C	21.590±1.238	3.485±0.225	0.008±0.001	8.756±0.349	0.239±0.026	3.539±0.113	0.869±0.107
Quenched at 400 °C	19.660±1.887	2.231±0.191	0.033±0.015	7.160±1.197	0.280±0.090	1.803±0.261	0.719±0.237

characteristics section, since the electrochemical charge transfer reaction is related closely to the number of active reaction sites, the small particle size and rough surface morphology induced by quenching increased the number of active reaction sites and decreased the resistance of the charge transfer reaction, leading to improvement of overall DSSC performance.

Conclusions

The effect of the quenching process on the performance of a TiO_2 photoelectrode for DSSCs was investigated. Introduction of the quenching step during sintering did not induce any change in the crystal structure or surface oxidation state of TiO_2 films. However, the quenching process significantly affected the microstructure and the surface morphology of TiO_2 films. The quenched TiO_2 films had smaller particles and rougher surface morphology compared to the furnace-cooled TiO_2 films. These microstructural and morphological changes were related to the overall DSSC performance. Based on UV-visible spectroscopy analysis, the amount of dye adsorption on the quenched TiO_2 films increased compared with that of the furnace-cooled TiO_2 films. In terms of the electrochemical reaction, microstructural and morphological changes such as small particle size and rough surface morphology caused by quenching increased the number of active reaction sites and consequently promoted the charge transfer reaction and diffusion process, improving overall DSSC performance.

Acknowledgements

This research was supported by the National Research Foundation of Korea (NRF) grant funded by the Korea government (MSIT) (No. 2020R1A2C1004580). This work was also supported by the Technology Development Program to Solve Climate Changes of the National Research Foundation (NRF) grant funded by the Korea government (Ministry of Science and ICT) (2017M1A2A2044930). This work was partly supported by Korea Institute of Energy Technology Evaluation and Planning (KETEP) grant funded by the Korea government (MOTIE) (20213030040110).

References

1. J. Gong, J. Liang, and K. Sumathy, Renew. Sustain. Energy Rev. 16[8] (2012) 5848-5860.
2. J. Gong, K. Sumathy, Q. Qiao, and Z. Zhou, Renew. Sustain. Energy Rev. 68 (2017) 234-246.
3. M.S. Ahmad, A.K. Pandey, and N.A. Rahim, Renew. Sustain. Energy Rev. 77 (2017) 89-108.
4. K. Sharma, V. Sharma, and S.S. Sharma, Nanoscale Res. Lett. 13[1] (2018) 381.
5. S. Thomas, T.G. Deepak, G.S. Anjusree, T.A. Arun, S.V. Nair, and A.S. Nair, J. Mater. Chem. A 2[13] (2014) 4474-4490.
6. K.H. Ko, Y.C. Lee, and Y.J. Jung, J. Colloid Interface Sci. 283[2] (2005) 482-487.
7. W. Wunderlich, T. Oekermann, L. Miao, N.T. Hue, S. Tanemura, and M. Tanemura, J. Ceram. Process. Res. 5[4] (2004) 343-354.
8. X. Feng, K. Shankar, O.K. Varghese, M. Paulose, T.J. Latempa, and C.A. Grimes, Nano Lett. 8[11] (2008) 3781-3786.
9. Y. Jiang, M. Li, R. Ding, D. Song, M. Trevor, and Z. Chen, Mater. Lett. 107 (2013) 210-213.
10. B.H. Lee, M.Y. Song, S.-Y. Jang, S.M. Jo, S.-Y. Kwak, and D.Y. Kim, J. Phys. Chem. C 113[51] (2009) 21453-21457.
11. J.M. Macak, H. Tsuchiya, A. Ghjcov, and P. Schmuki, Electrochem. Commun. 7[11] (2005) 1133-1137.
12. S.I. Noh, T.-Y Seong, and H.J. Ahn, J. Ceram. Process. Res. 13[4] (2012) 491-494.
13. J. Navas, C. Fernadez-Lorenzo, T. Agulilar, R. Alcantara, and J. Martin-Calleja, Phys. Status Solidi A 209[2] (2012) 378-385.
14. Q. Liu, Y. Zhou, Y. Duan, M. Wang, and Y. Lin, Electrochim. Acta 95 (2013) 48-53.
15. M.S. Mahmoud, M.S. Akhtar, I.M.A. Mohamed, R. Hamdan, Y.A. Dakka, and N.A.M. Barakat, Mater. Lett. 225 (2018) 77-81.
16. P. Wang, S.M. Zakeeruddin, J.E. Moser, R. Humphry-Baker, P. Comte, V. Aranyos, A. Hagfeldt, M. K. Nazzeruddin, and M. Gratzel, Adv. Mater. 16[20] (2004) 1806-1811.
17. W. Zeng, Y. Cao, Y. Bai, Y. Wang, Y. Shi, M. Zhang, F. Wang, C. Pan, and P. Wang, Chem. Mater. 22[5] (2010) 1915-1925.
18. S. Chinnasamy and S. Ramanathan, J. Ceram. Process. Res. 21[1] (2020) 123-130.
19. C.M. Elliott, Nat. Chem. 3[3] (2011) 188-189.
20. P. Wang, S.M. Zakeruddin, I. Exnar, and M. Gratzel, Chem. Commun. 24 (2002) 2972-2973.
21. M.-J. Jeng, Y.-L. Wung, L.-B. Chang, and L. Chow, Int. J. Photoenergy 2013 (2013) Article ID 563897.
22. Y.J. Son, J.S. Kang, J.J. Yoon, J. Kim, J.W. Jeong, J.H. Kang, M.J. Lee, H.S. Park, and Y.-E. Sung, J. Phys. Chem. C 122[13] (2018) 7051-7060.
23. W.Y. Park and K.T. Lee, J. Ceram. Process. Res. 22[5] (2021) 584-589.
24. S. Ito, P. Chen, P. Comte, M. K. Nazeeruddin, P. Liska, P. Pechy, and M. Gratzel, Prog. Photovolt.: Res. Appl. 15[7] (2007) 603-612.
25. A.I. Kontos, A.G. Kontos, D.S. Tsoukleris, M.-C. Bernard, N. Spyrellis, and P. Falaras, J. Mater. Process. Technol. 196[1-3] (2008) 243-248.
26. B. Roose, S. Pathak, and U. Steiner, Chem. Soc. Rev. 44[22] (2015) 8326-8349.
27. R. Sanjines, H. Tang, H. Berger, F. Gozzo, G. Margaritondo, and F. Levy, Int. J. Appl. Phys. 75[6] (1994) 2945-2951.
28. B. O'Regan and M. Gratzel, Nature 353[6346] (1991) 737-740.
29. Y.J. Kim, M.H. Lee, H.J. Kim, G. Lim, Y.S. Choi, N.-G. Park, K.K. Kim, and W.I. Lee, Adv. Mater. 21[36] (2009) 3668-3673.
30. R. Govindaraj, M.S. Pandian, P. Ramasamy, and S. Mukhopadhyay, Bull. Mater. Sci. 38[2] (2015) 291-296.
31. T.P. Chou, Q. Zhang, B. Russo, G.E. Fryxell, and G. Cao, J. Phys. Chem. C 111[17] (2007) 6296-6302.
32. K.S. Park, Q. Zhang, D. Myers, and G. Cao, ACS Appl. Mater. Interfaces 5[3] (2013) 1044-1052.
33. S. Nakade, Y. Saito, W. Kubo, T. Kanzaki, T. Kitamura, Y. Wada, and S. Yanagida, Electrochem. Commun. 5[9] (2003)

804-808.
34. S. Nakade, Y. Saito, W. Kubo, T. Kitamura, Y. Wada, and S. Yanagida, J. Phys. Chem. B 107[33] (2003) 8607-8611.
35. S.C. Yang, D.J. Yang, J.K. Kim, J.M. Hong, H.G. Kim, and I.D. Kim, Adv. Mater. 20 (2008) 1059-1064.
36. S. Muduli, O. Game, V. Dhas, K. Vijayamohanan, K.A. Bogle, N. Valanoor, and S.B. Ogale, Solar Energy 86[5] (2012) 1428-1434.
37. K. Guo, M. Li, X. Fang, X. Liu, B. Sebo, Y. Zhu, Z. Hu, and X. Zhao, J. Power Source 230 (2013) 155-160.
38. N. Chander and M.R. Samantaray, IEEE J. Photovoltaics 11[5] (2021) 1213-1221.
39. C.A. Leach, P. Tanev, and B.C.H. Steele, J. Mater. Sci. Lett. 5[9] (1986) 893-894.
40. K. Niesz, T. Ould-ely, H. Tsukamoto, and D.E. Morse, Ceram. Int. 37[1] (2011) 303-311.
41. . Zhang, J. Zheng, Y. Liu, C. Zhang, W. Hao, Z. Lei, and M. Tian, Mater. Res. Bull. 115 (2019) 49-54.
42. .C. Maurya, S. Senapati, S. Singh, P. Srivastava, P. Maiti, and L. Bahadur, Chemistry Select. 3[34] (2018) 9872-9880.
43. M.J. Jeng, Y.L. Wung, L.B. Chang, and L. Chow, Int. J. Photoenergy 2013 (2013) Article ID 280253.
44. V.A. González-Verjan, B. Trujillo-Navarrete, R.M. Félix-Navarro, J.D. de León, J.M. Romo-Herrera, J.C. Calva-Yáñez, J. M. Hernández-Lizalde, and E.A. Reynoso-Soto, Mater. Renew. Sustain. Energy 9 (2020) 1-8.
45. Z.S. Wang, H. Kawauchi, T. Kashima, and H. Arakawa, Coord. Chem. Rev. 248[13-14] (2004) 1381-1389.
46. S.N. Karthick, K.V. Hemalatha, C.J. Raj, H.-J. Kim, and M. Yi, J. Ceram. Process. Res. 13[S1] (2012) 136-139.
47. A. Aboulouard, B. Gultekin, M. Can, M. Erol, A. Jouaiti, B. Elhadadi, C. Zafer, and S. Demic, J. Mat. Res. Tech. 9[2] (2020) 1569-1577.
48. Y. Kim, B.J. Yoo, R. Vittal, Y. Lee, N.-G. Park, and K.-J. Kim, J. Power Sources 175[2] (2008) 914-919.
49. D. Kim, K. Lee, H. Lee, J. Lim, and J. Park, J. Kor. Cryst. Growth and Cryst. Tech. 30[2] (2020) 61-65.
50. C.-P. Hsu, K.-M. Lee, J.T.-W. Huang, C.-Y. Lin, C.-H. Lee, L.-P. Wang, S.-Y. Tasi, and K.-C. Ho, Electrochim. Acta 53[25] (2008) 7514-7522.
51. R. Kern, R. Sastrawan, J. Ferber, R. Stangl, and J. Luther, Electrochim. Acta 47[26] (2002) 4213-4225.
52. S. Sarker, A.J.S. Ahammad, H.W. Seo, and D.M. Kim, Int. J. Photoenergy 2014 (2014) Article ID 851705.